

Mach number effect on the instability of a planar interface subjected to a rippled shockWenbin Zhang,¹ Qiang Wu,¹ Liyong Zou,³ Xianxu Zheng,¹ Xinzhu Li,¹ Xisheng Luo,² and Juchun Ding^{2,*}¹Laboratory for Shock Wave and Detonation Physics, Institute of Fluid Physics, China Academy of Engineering Physics, Mianyang, Sichuan 621900, China²Advanced Propulsion Laboratory, Department of Modern Mechanics, University of Science and Technology of China, Hefei 230026, China³Mechanical Engineering, Physical Science and Engineering Division, King Abdullah University of Science and Technology, Thuwal 23955-6900, Saudi Arabia

(Received 14 June 2018; published 12 October 2018)

The Richtmyer-Meshkov (RM) instability of a planar interface (N_2 - SF_6) subjected to a sinusoidal rippled shock, as the variant of a sinusoidal interface impinged by a planar shock, is investigated through high-order compressible multicomponent hydrodynamic simulations. The rippled shock is generated by a planar shock penetrating through a single-mode interface (He - N_2), and its propagation characteristic agrees reasonably with Bates' analytical solution. Evolution of the flat contact surface impacted by the rippled shock is found to be heavily dependent on the rippled shock phase, and it can be well explained by the impulsive perturbation and continuous perturbation regimes. Various rippled shocks with different Mach numbers ranging from 1.15 to 1.80 are considered. It is found that the influence of the shock strength on the instability growth behaves differently for rippled shocks at different phases. In the case that the shock-interface collision happens when the rippled shock amplitude vanishes for the first time, as the shock strength increases, the impulsive perturbation (i.e., amplitude growth caused by the impulsive shock impact) plays an increasingly more important role in the instability growth than the continuous perturbation (i.e., amplitude growth induced by the disturbed postshock pressure field). In contrast, in the case that the impingement occurs when the rippled shock amplitude becomes zero for the second time, the instability development contributed by the impulsive perturbation is a certain percentage of the total instability growth regardless of the shock strength. The role of the impulsive perturbation in the present nonstandard RM instability within the single-mode framework can be reasonably predicted by an empirical formula combined with the model of Ishizaki *et al.* [*Phys. Rev. E* **53**, R5592 (1996)].

DOI: [10.1103/PhysRevE.98.043105](https://doi.org/10.1103/PhysRevE.98.043105)**I. INTRODUCTION**

The development of a corrugated interface separating two different fluids subjected to a shock wave is often referred to as the Richtmyer-Meshkov (RM) instability, which was first theoretically analyzed by Richtmyer [1] and later experimentally confirmed by Meshkov [2]. After the shock passage, the interface deforms continually along with the growth of its perturbation amplitude. As time proceeds, secondary instabilities become pronounced and massive small-scale vortices are generated along the interface, which later induce the turbulent mixing. Over the past decades, this hydrodynamic instability has been extensively studied through experiments [3–6], simulations [7–9], and theoretical analyses [10–12] due to its important role in academic research, e.g., compressible turbulence [13] and engineering applications such as inertial confinement fusion (ICF) [14].

In the study of the RM instability, much attention has been devoted to the problem of a uniform shock interacting with a perturbed interface [15,16]. However, this is not the case for many scenarios where the incident shock is a rippled one. For example, in ICF, the nonuniform laser irradiation and the target surface roughness may produce considerable perturbations on the generated imploding shock [14,17]. Also, in

supernovae, the radially expanding shock is always perturbed as it passes through the corrugated layers between different materials [18]. As an analog of the standard RM instability (a uniform shock accelerating a perturbed interface), the instability of a uniform interface impacted by a rippled shock has seldom been investigated.

Ishizaki *et al.* [17] first performed a numerical simulation of this instability where the rippled shock was produced by a constantly moving rippled piston. It was found that the impulsive nonuniform and continuous pressure perturbations are the main regimes leading to the instability growth. The instability development at an initially flat interface by a rippled shock impact was also observed in a laser experiment [19], and the growth rate was in reasonable agreement with the simulation result. This hydrodynamic instability has also been examined by our recent shock-tube experiments in both planar and cylindrical geometries [20–22], in which the rippled shock is produced by a uniform shock diffracting over single or multiple cylinders. It was found that the interface evolution was significantly influenced by the number, spacing, and relative position of the cylinders, and a much smaller growth rate compared to the standard counterpart was observed. Recently, Zhou has specially discussed this nonstandard RM instability in his review paper [15].

In our previous experiments, the rippled shock can be conveniently produced by the diffraction of a uniform incident shock around a cylinder [20–22], but the resulting wave

*djcd@mail.ustc.edu.cn

patterns as well as the rippled shock characteristics are quite complex. As a result, the interfacial evolution is continually influenced by the complex pressure field caused by the shock-shock interaction, and the analysis of the main physical mechanism of this instability becomes very difficult. As a follow-up study, in this work, a rippled shock with a simple sinusoidal shape impacting a flat N_2 - SF_6 interface is studied by two-dimensional (2D) high-resolution numerical simulations. The rippled shock is created by a planar shock transmitting a single-mode He- N_2 interface. The simpler shock configuration as well as the cleaner flow field produced here facilitates a deeper analysis of this nonstandard RM instability. The influences of the rippled shock phase and strength on the instability development are specially discussed.

II. NUMERICAL METHOD AND VALIDATION

A. Numerical method and physical model

In this study, we are mainly concerned with the instability development at early to intermediate stages when the flow is dominated by the large-scale structures, such that the influences of the viscosity, heat transfer, and molecular mixing can be neglected. The compressible multicomponent Euler equations augmented by the γ -model based on the ideal gas assumption are adopted as the control system. The shock- and interface-capturing algorithms are employed to track the motion of the density discontinuities such as the shock wave, the contact surface, and the fluid interface. In a quasiconservative form, the governing equations can be written as

$$\begin{aligned} \frac{\partial \rho}{\partial t} + \frac{\partial \rho u_j}{\partial x_j} &= 0, \\ \frac{\partial \rho u_i}{\partial t} + \frac{\partial \rho u_j u_i}{\partial x_j} + \frac{\partial p}{\partial x_i} &= 0, \\ \frac{\partial E}{\partial t} + \frac{\partial (E + p) u_j}{\partial x_j} &= 0, \\ \frac{\partial}{\partial t} \left(\frac{1}{\gamma - 1} \right) + u_j \frac{\partial}{\partial x_j} \left(\frac{1}{\gamma - 1} \right) &= 0. \end{aligned} \quad (1)$$

Here i and j denote the i th and j th directions, respectively, and ρ , u_k , and p stand for the density, velocity, and pressure, respectively. E is the total energy, and γ the specific heat ratio.

In the 2D Cartesian coordinate, the primitive variables ρ , u_k , p , and $1/(\gamma - 1)$ are reconstructed in the characteristic space by a fifth-order weighed essential nonoscillatory (WENO) scheme, and the numerical fluxes at the cell boundaries are calculated by the Harten-Lax-van Leer-Contact (HLLC) approximate Riemann Solver. A third-order total variation diminished (TVD) Runge-Kutta scheme is used for the temporal advancement. More details about the present algorithm can be found in previous studies [23–25]. Although the two materials are assumed to be immiscible, artificial mixing between them in the vicinity of the interface would be inevitably introduced by the numerical dissipation. It should be mentioned that the numerical treatment considering an artificial mixture of gases as a single gas with an averaged adiabatic index does not essentially influence the accuracy of the numerical solution. The present physical model and numerical algorithm have been widely used in the simulations

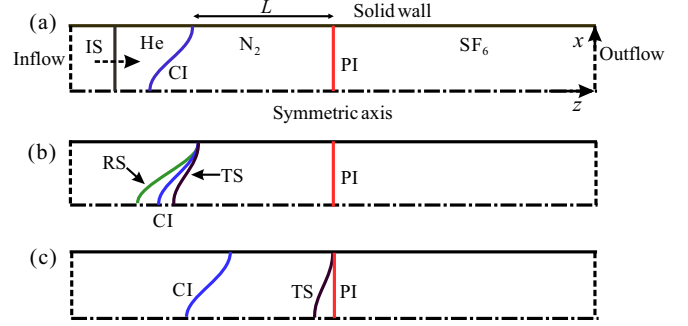


FIG. 1. Schematic of the flow configurations at (a) the initial state, (b) the time moment when the incident shock (IS) completely passes across the contact interface (CI), and (c) the moment when the transmitted shock (TS) encounters the planar interface (PI). RS is the reflected shock.

of compressible multicomponent and multiphase flows and showed a good performance [26–29].

Figure 1 depicts the computational flow configuration, in which a planar incident shock (IS), a sinusoidal contact interface (CI) between He and N_2 , and a planar interface (PI) separating N_2 and SF_6 are initially set. The IS with a Mach number of M_{IS} is located upstream of the CI. The sinusoidal interface can be expressed as $z = a_0 \sin(kx + \pi/2)$, where a_0 and k are, respectively, the initial amplitude and wave number. Note that $k = \pi/50 \text{ mm}^{-1}$ and $a_0 = 5.0 \text{ mm}$ are adopted for simulations throughout this work. Due to the symmetry of the flow, only the upper half of the physical space is chosen as the computational domain with an area of $x \times z = 50 \times 500 \text{ mm}^2$, which is discretized by 250×2500 uniform grids. The initial postshock quantities are calculated according to the Rankine-Hugoniot relation. The left and right boundaries are treated as inflow and outflow, respectively. The top boundary is solid wall, and the bottom one is set as symmetric. The simulations are conducted at an environmental pressure of 101.325 kPa and temperature of 293.15 K. The properties of the test gases (He, N_2 , and SF_6) are listed in Table I.

As the simulation starts, the incident shock moves downstream and then passes across the contact interface, bifurcating into a rippled reflected (RS) and transmitted shock (TS), as shown in Fig. 1(b). During the shock-interface interaction, the sinusoidal perturbation of the CI is gradually transferred to the TS due to the acoustic impedance mismatch across the interface. The generated TS possesses an initial amplitude of $a_{S0} = (1 - W_{TS}/W_{IS})a_0$ and a Mach number of M_S , where W_{IS} and W_{TS} represent the velocities of the IS and TS, respectively. Since the strength of a rippled shock is nonuniform along its front, in this work, the TS strength is defined based on the zero-order variable as the linear analysis of Bates [30]. The time duration for the IS traversing the perturbed CI is

TABLE I. Properties of the ambient He, N_2 , and SF_6 .

| Gas | Density (kg/m^3) | Specific heat ratio γ |
|--------|-----------------------------|------------------------------|
| He | 0.166 | 1.667 |
| N_2 | 1.164 | 1.399 |
| SF_6 | 6.143 | 1.094 |

TABLE II. Parameters of the flow conditions for different Mach number cases.

| Case | 1 | 2 | 3 | 4 |
|------------------------------|---------|---------|---------|---------|
| M_{IS} | 1.10 | 1.22 | 1.30 | 1.50 |
| M_S | 1.15 | 1.34 | 1.47 | 1.80 |
| a_{S0} (mm) | 3.18 | 3.09 | 3.04 | 2.92 |
| W_{IS} (ms ⁻¹) | 1108.20 | 1229.09 | 1309.69 | 1511.18 |
| W_{TS} (ms ⁻¹) | 402.72 | 469.23 | 514.42 | 629.30 |
| u_I (ms ⁻¹) | 53.43 | 112.53 | 149.60 | 236.67 |

$\Delta t = 2a_0/W_{IS}$. As the TS propagates forward, its amplitude (a_s) oscillates and decays gradually. Later, as the distorted TS hits the PI, the PI is immediately accelerated to a velocity of u_I [Fig. 1(c)], and then the instability develops evidently on it.

B. Dynamics of the sinusoidal rippled shock

Before exploring the rippled shock-induced instability, the dynamics of the rippled shock generated is first examined (remove the PI in Fig. 1). Four rippled shocks with

different Mach numbers ranging from 1.15 to 1.80 are generated by changing the incident shock strength from 1.10 to 1.50. The detailed parameters are listed in Table II, where the variables W_{IS} , W_{TS} , and M_S are calculated based on the one-dimensional gas dynamics. It is seen that although the amplitude of the CI remains invariable, there is still a slight discrepancy in the generated rippled shock amplitude among different cases. Considering that the deviation of shock amplitude in each case from the averaged value is within 5%, the influence of the initial shock amplitude on the instability growth can be neglected in this study.

Temporal variation of the rippled shock amplitude (a_s), which is defined as half of the distance between the shock crest and trough [Fig. 1(c)], is displayed in Fig. 2 where the theoretical prediction of Bates [30] is given for comparison. Generally, reasonable agreement between the simulation and the prediction is obtained. As for the $M_S = 1.80$ case, there is a visible difference in the shock propagation between the simulation and theory at the early stage. A possible reason is that in Bates' theory [30] the nonuniform pressure field behind the initial rippled shock has not been taken into account. This simplification produces only a negligible influence on

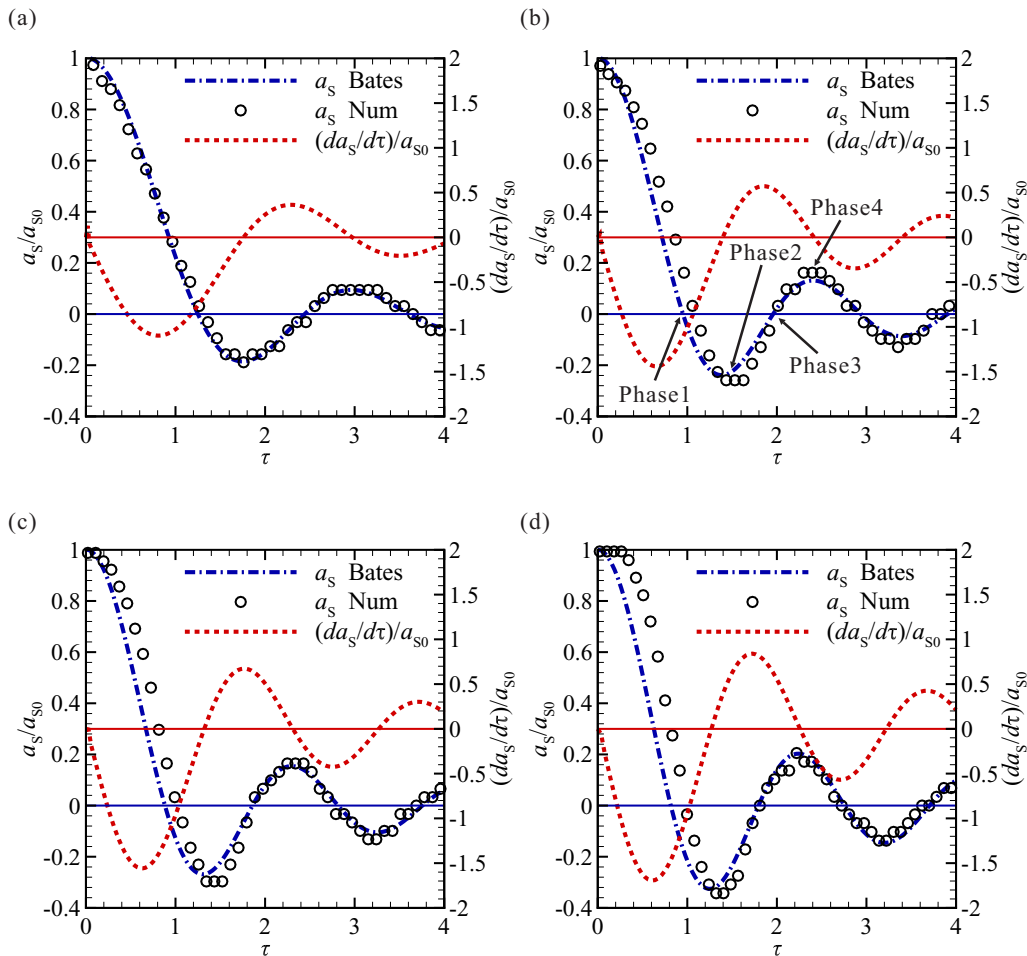


FIG. 2. Evolution of the ratio between the generated shock amplitude and its initial value as well as dimensionless variations of the amplitude growth rate of a rippled shock versus time under a Mach number of (a) $M_S = 1.15$, (b) $M_S = 1.34$, (c) $M_S = 1.47$, and (d) $M_S = 1.80$. The time is scaled as $\tau = tW_{TS}/\lambda$ where λ is the wavelength of the perturbation. The dash-dot and dash lines denote, respectively, the variations of the shock amplitude and growth rate predicted by Bates [30], and the open circle represents the present numerical result. The blue and red horizontal lines indicate a zero value of a_s and da_s/dt , respectively.

the propagation of weak shocks but becomes quite influential for relatively stronger shocks. As the rippled shock travels a certain distance, the discrepancy diminishes gradually, and a good agreement is obtained again. Note that the “kink” in the $M_S = 1.80$ case shortly after $\tau = 0$ is independent of the grid size and mainly caused by the compressibility effect. For all cases, the perturbation amplitude of the rippled shock oscillates and decays gradually, leading to a periodic variation of the shock phase. The good agreement between the simulation and Bates’ prediction demonstrates that the present method of a planar shock transmitting a single-mode density interface can produce a perfectly single-mode rippled shock. Dimensionless variation of the amplitude growth rate versus time is also given in Fig. 2. As can be seen, during the first reduction of the shock amplitude from its initial value to zero (phase 1), the corresponding amplitude growth rate drops continually from zero to nearly a negative extreme value. As the amplitude increases from a negative to zero again (phase 3), the growth rate reaches a positive extreme point. Nevertheless, as a minimum (phase 2) or maximum shock amplitude (phase 4) is reached, the growth rate becomes zero. The correlation between the shock amplitude and the growth rate would be useful to explain the dependence of the rippled shock-induced interfacial instability on the shock phase discussed hereinafter. It is also found that both the local extreme values and the oscillation frequency of the amplitude growth rate rise as the Mach number increases, implying that a stronger rippled shock experiences a more prominent oscillation.

III. RESULTS AND DISCUSSION

A. Influence of rippled shock phase

The instability of a planar N_2 - SF_6 interface impacted by a rippled shock of $M_S = 1.34$ at four different phases is first considered. As indicated in Fig. 2(b), phases 1 and 3 correspond to the instants when $a_S = 0$, and phases 2 and 4 to the moments when a_S reaches, respectively, a maximum and a minimum. By moving the location of the PI (i.e., changing the distance between the PI and CI), four rippled shocks with respectively phases 1–4 just before their interaction with the PI are obtained. Time origin in this work is defined as the moment when the sinusoidal rippled shock contacts the PI.

Figure 3 displays the density contours at $\tau = 10$ for the flat N_2 - SF_6 interface subjected to a rippled shock at four different phases. As we can see, for rippled shocks at phases 1 and 3 when the perturbation amplitude is nearly zero, the PI distorts evidently after the shock impact, and the signs of the perturbation amplitudes for the two cases are opposite. Nevertheless, no visible perturbation growth can be found at the PI for the phase-2 and -4 cases where the rippled shock possesses a considerable initial distortion. The dynamics of rippled shock-induced instability exhibits a great distinction from the standard counterpart, and its physical mechanism will be illustrated later. The perturbation amplitude and the corresponding growth rate for the distorted interface are, respectively, defined as

$$a_1 = \frac{1}{2}(z_{BP} - z_{MP}), \quad (2)$$

$$\frac{da_1}{dt} = \frac{1}{2}(u_{zBP} - u_{zMP}). \quad (3)$$

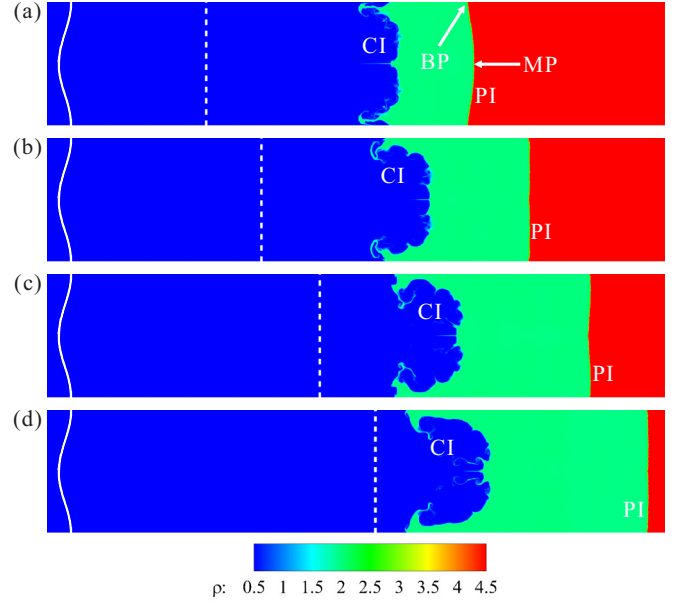


FIG. 3. Density contour images at $\tau = 10$ for a rippled shock at (a) phase 1, (b) phase 2, (c) phase 3, and (d) phase 4. BP and MP are, respectively, the boundary and middle points of the deformed planar interface (PI). The dash and solid lines denote the initial locations of the planar interface and contact interface (CI), respectively.

Here z_{BP} and z_{MP} are the z -component positions of the boundary (BP) and middle points (MP), respectively, and u_{zBP} and u_{zMP} are the corresponding z -component velocities. Temporal variations of the perturbation amplitude and the growth rate for the four cases are depicted in Fig. 4. The rippled shock at phase 1 is found to induce the fastest instability growth at the PI among all the cases, and the phase-3 shock causes a relatively slower instability growth. For the phase-2 and -4 cases, no evident instability development can be found, and thus the perturbation amplitude remains zero with time. For all cases, the perturbation growth rate oscillates at early stages and then approaches an asymptotic value. The asymptotic growth rate is negative for the phase-1 case, positive for phase 3, and approximately zero for phases 2 and 4. This finding is consistent with the interfacial evolution as shown in Fig. 3. As we know, for the standard RM instability, no perturbation growth appears after a planar shock strikes a flat density interface. Nevertheless, this is not the case for the present nonstandard counterpart where although the shock is initially planar (phases 1 and 3), the interface suffers a considerable instability growth after the shock impact. This indicates a great difference in the physical regimes between the two types of RM instabilities.

B. Influence of shock strength

Next we investigate the dependence of the instability growth on the shock strength under a fixed shock phase. Four rippled shocks with different Mach numbers ranging from 1.15 to 1.80 are employed, as listed in Table II. First, these rippled shocks are set to be in phase 1 ($a_S = 0$) at the time when they meet the PI, and hence induce a considerable instability growth. The density contours at $\tau = 10$ for a uniform interface

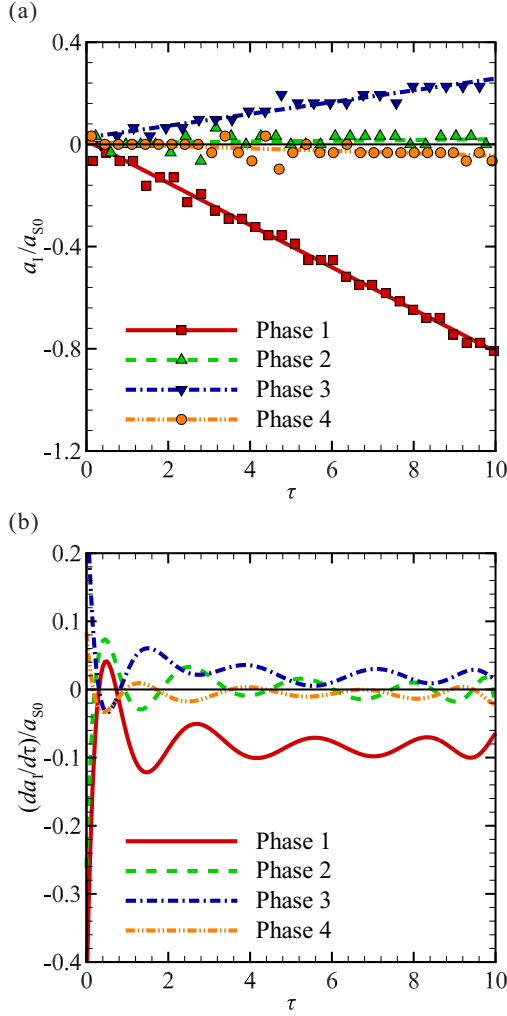


FIG. 4. Dimensionless variations of the amplitude (a) and the amplitude growth rate (b) of the PI versus time for different shock phase cases. The dimensionless time follows the same normalization method as that in Fig. 2.

subjected to a rippled shock with different strengths are shown in Fig. 5. It is seen that as the incident shock becomes stronger, the CI and PI move faster and the N_2 region suffers a greater degree of compression. More importantly, a stronger rippled shock is able to induce a much quicker instability growth. For the $M_S = 1.80$ case, some small-scale structures emerge at the PI, which is mainly ascribed to the coupling effect between the deformed PI and CI (close to each other this case). We have also considered higher Mach number cases, including $M_S = 2.0$, 2.2 , and 2.5 . It is found that the two interfaces are closer to each other as the Mach number increases, and consequently, the coupling effect between the interfaces is more evident, producing numerous small-scale structures. Since the amplitude of the small-scale structures with higher modes becomes comparable to the amplitude of the initial long-wavelength interface, the single-mode assumption breaks down. Hence, the rippled shock strength considered in this work is limited to weak to moderate range ($M_S \leq 1.80$). Figure 6 shows the temporal variations of the perturbation amplitude and growth rate in a dimensionless form. For each shock strength,

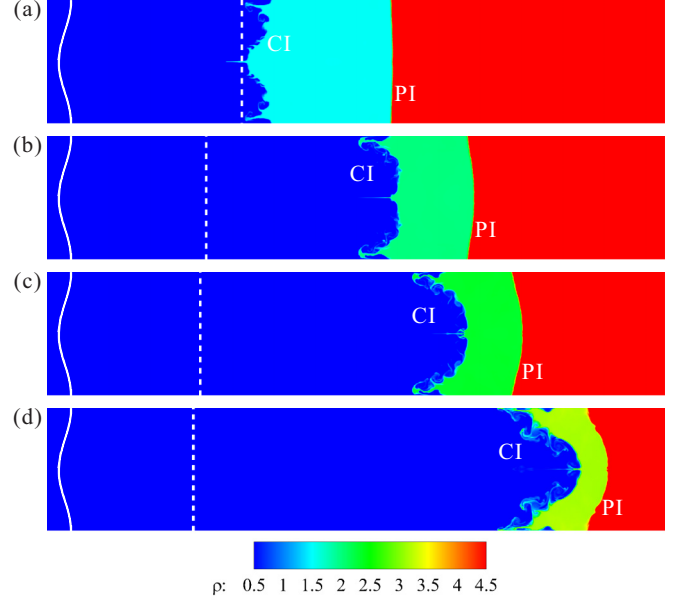


FIG. 5. Density contour images at $\tau = 10$ for the phase-1 rippled shocks with different Mach numbers: (a) $M_S = 1.15$, (b) $M_S = 1.34$, (c) $M_S = 1.47$, and (d) $M_S = 1.80$. The dash and solid lines are the initial positions of the PI and CI, respectively.

the perturbation amplitude grows approximately linearly with time, and no evident saturation of the linear growth is observed. Also, the growth rate oscillates at the early stage and then asymptotically approaches a constant value, which rises greatly as the shock Mach number increases.

According to the analysis of Ishizaki *et al.* [17], the development of this nonstandard RM instability is mainly attributed to the impulsive perturbation by the rippled shock impact and the continual pressure perturbation behind the rippled shock. The impulsive perturbation at the contact surface is found to be closely related to the growth rate of the rippled shock amplitude, as described by

$$\left(\frac{da_1}{dt}\right)_{t=0} = \frac{u_1}{W_{TS}} \left(\frac{da_S}{dt}\right)_{t=0}. \quad (4)$$

Assuming the pressure perturbation behind the rippled shock is a damped oscillation, the perturbation growth contributed by the pressure perturbation can be approximately calculated by $g(t) = \Delta g e^{-\Psi t} \sin(\omega t + \phi)$, where ϕ is the shock phase at $t = 0$, Δg is the acceleration, and ω and Ψ ($\Psi \ll \omega$) are the frequency and acceleration damping rate, respectively. Then a theoretical model to estimate the asymptotic growth rate is developed, which is expressed as

$$\begin{aligned} \left(\frac{da_1}{dt}\right)_{t \rightarrow \infty} &= \frac{u_1}{W_{TS}} \left(\frac{da_S}{dt}\right)_{t=0} - \int_0^\infty g(t) dt \\ &= \frac{u_1}{W_{TS}} \left(\frac{da_S}{dt}\right)_{t=0} - \frac{\Delta g}{\omega} \cos \phi. \end{aligned} \quad (5)$$

Here $(da_S/dt)_{t=0}$ denotes the growth rate of the shock amplitude at the impacting moment, and it can be readily obtained from the simulation result as shown in Fig. 2.

Figure 7 depicts the pressure distributions along the symmetry axis at different time instants ($\tau = 0.1$, 0.2 , and 0.3)

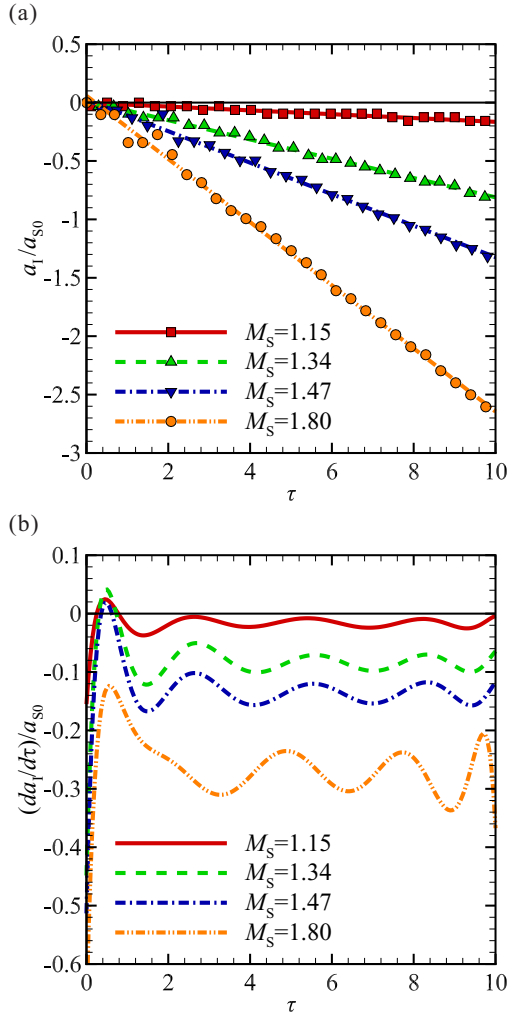


FIG. 6. Dimensionless variations of the amplitude (a) and the amplitude growth rate (b) of the PI versus time for a rippled shock at phase 1 with different strengths.

for the PI subjected to a rippled shock at phases 1, 2, and 3. After the TS-PI interaction, a second transmitted (STS) and

a reflected shock (SRS) are formed, and both present a sinusoidal-like shape. As the distorted STS and SRS move, respectively, downstream and upstream, the pressure profile between them varies continually with time. At the beginning ($\tau = 0.1$), the pressure gradient at the PI is positive for the phase-1 and -2 cases but negative for the phase 3. As indicated in Fig. 2(b), $(d^2a_S/dt^2)_{t=0}$ is also positive for the phase-1 and -2 circumstances and negative for the phase 3. This detailed flow field information confirms the previous theoretical analysis that $(d^2a_S/dt^2)_{t=0}$ has the same phase with $(\partial p/\partial z)_{z=z_1} \sim g(t=0) \sim \Delta g \sin\phi$ [17], where z_l is the z -component position of the interface. Based on this, it can be easily deduced that $(da_S/dt)_{t=0}$ is always in phase with $(\Delta g/\omega)\cos\phi$. This clearly explains the fact that the whole perturbation growth caused by the impulsive perturbation and oscillatory-damped pressure perturbation is heavily dependent on the phase of the rippled shock at the time when it hits the interface, as observed in Fig. 3.

Figure 8 shows the distributions of the pressure and pressure gradient along the symmetry axis at $\tau = 0.1$ for different Mach number cases. As we can see, the pressure gradient at the PI rises as the shock is intensified. Based on the fact that $(\partial p/\partial z)_{z=z_1} \sim g(t=0) \sim \Delta g \sin\phi$ is in phase with the incident rippled shock, we can get $(\partial p/\partial z)_{z=z_1} \sim \Delta g$. It means that the pressure perturbation acceleration Δg grows as the shock Mach number increases. As found from Fig. 2, the Mach number increment also leads to a rise in $(d^2a_S/dt^2)_{t=0}$, which indicates that the impulsive perturbation increases with the Mach number as well. These findings well explain the growth rate dependence on the shock strength shown in Fig. 5.

Then four rippled shocks of different Mach numbers at phase 3 are considered. Temporal variations of the perturbation amplitude and the growth rate for a uniform N_2 - SF_6 interface subjected to four such rippled shocks are shown in Fig. 9. For all cases, the instability growth follows a linear regime but with a growth rate much smaller than the phase-1 case. It is found that as the incident shock strength is varied from 1.15 to 1.47 the growth rate increases continually, whereas when M_S is increased from 1.47 to 1.80 the growth rate even suffers a little decrease. The main reason is that in the present simulations when the initial shock becomes

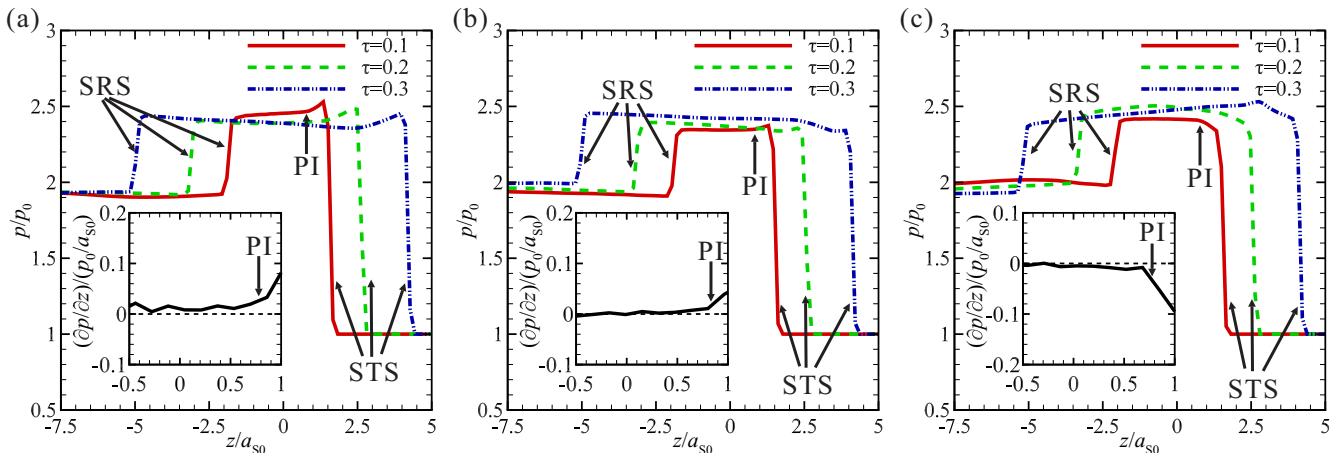


FIG. 7. Pressure distributions along the symmetry axis for the PI subjected to a rippled shock of $M_S = 1.34$ at (a) phase 1, (b) phase 2, and (c) phase 3. The inserted figures show the pressure gradients in the vicinity of the evolving PI at $\tau = 0.1$.

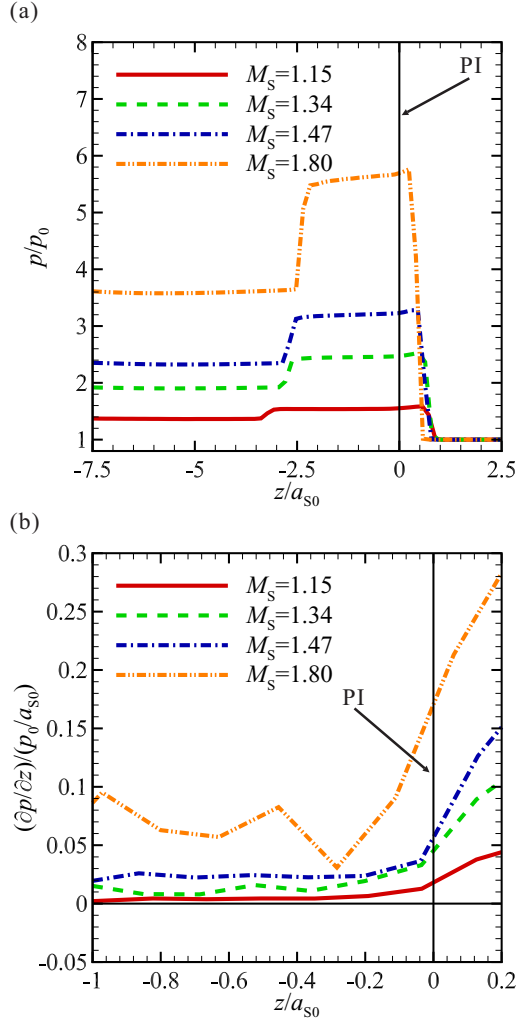


FIG. 8. The distributions of the pressure (a) and pressure gradient (b) along the symmetry axis in the vicinity of the evolving PI for the different Mach number cases at $\tau = 0.1$.

stronger, the shocked CI and PI are closer to each other, and, consequently, the coupling effect between them starts to act. Especially, for phase-3 cases with a relatively slower instability growth, such a coupling effect may significantly influence the whole instability development. Thus, the data for the $M_S = 1.80$ case are contaminated and cannot be used in the following analysis. For rippled shocks at phases 2 and 4, no visible perturbation growth on the shocked interface can be observed, which is ascribed to the zero value of the impulsive and continuous pressure perturbations at the impacting moment, and the corresponding results are not shown again.

Let $1 - \varepsilon$ represent the ratio of the continuous pressure perturbation to the impulsive perturbation,

$$1 - \varepsilon = \left(\frac{\Delta g}{\omega} \cos \phi \right) / \left[\frac{u_1}{W_{TS}} \left(\frac{da_S}{dt} \right)_{t=0} \right], \quad (6)$$

where ε is a dimensionless parameter. Then Eq. (5) can be written as

$$\left(\frac{da_1}{dt} \right)_{t \rightarrow \infty} = \varepsilon \frac{u_1}{W_{TS}} \left(\frac{da_S}{dt} \right)_{t=0}. \quad (7)$$

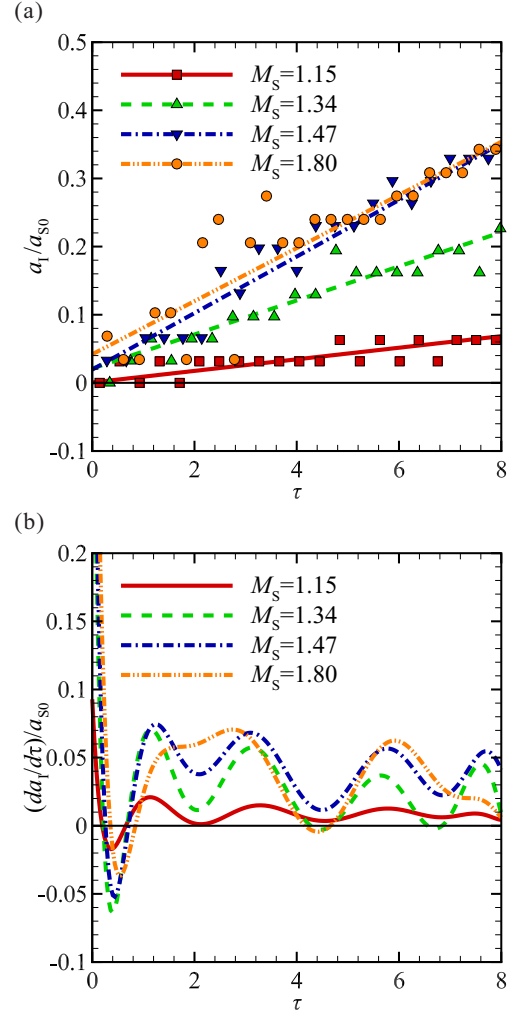


FIG. 9. Dimensionless variations of the normalized amplitude (a) and growth rate (b) versus the time for a rippled shock at phase 3 with different Mach numbers.

In the work of Ishizaki *et al.* [17], the parameter ε was found to be a constant (0.66) for various cases with different Atwood numbers and rippled shock phases under a fixed shock strength ($M_S = 2.0$). Here the Atwood number is defined as $A = (\rho_2 - \rho_1)/(\rho_2 + \rho_1)$, with ρ_1 and ρ_2 being the densities of the gases on the left- and right-hand sides of the interface, respectively. It means that the instability development contributed by the impulsive perturbation occupies a certain percentage (0.34) of the total instability growth regardless of the Atwood number and shock phase.

With a physical intuition that this rule may not be applicable for cases of different shock strengths, here we conduct a careful study on the dependence of ε on the rippled shock intensity. With the known quantities including the asymptotic growth rate (Figs. 6 and 9), the variables (Table II), and the growth rate of the rippled shock amplitude (Fig. 2), ε can be readily calculated for each case. The variation of the ε versus the shock Mach number is shown in Fig. 10. Note that in addition to the four different Mach numbers of the rippled shock considered above, another two Mach number cases ($M_S = 1.25$ and 1.60) are also supplemented. It is found

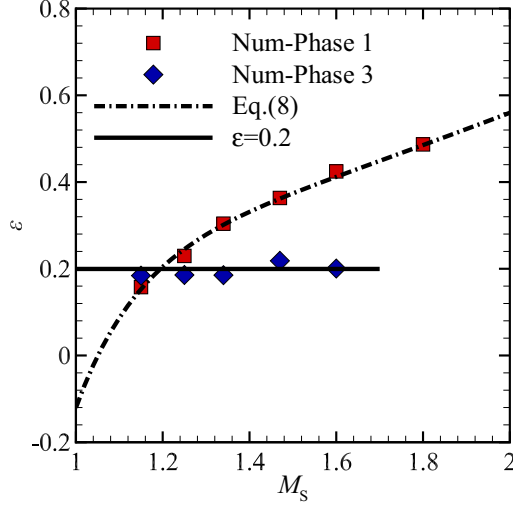


FIG. 10. Variation of the parameter ε versus the shock Mach number. The dash-dot line denotes the empirical prediction of Eq. (8), and the gradients and deltas refer to the present numerical results under a rippled shock at phases 1 and 3, respectively.

that for rippled shocks at phase 1, ε increases continually with the Mach number. This indicates that as the rippled shock becomes stronger, the impulsive perturbation plays a more and more important role in the instability growth. In all cases the relation of $1 - \varepsilon < 1$ is satisfied, which demonstrates that the impulsive perturbation contributes more to the instability growth than the continuous pressure perturbation. Also, $\varepsilon < 1$ is required to ensure a positive value of $1 - \varepsilon$. Since it has been found that ε is not sensitive to the Atwood number [17], we can assume ε as a power series of M_S :

$$\varepsilon = \sum_{k=0}^{\infty} A_k M_S^{-k}. \quad (8)$$

Here the coefficients A_k can be estimated by the curve fitting based on the numerical results, and we have $A_0 = 2.94$, $A_1 = -9.55$, $A_2 = 12.69$, and $A_3 = -6.20$. The solution of Eq. (8) is then compared with the numerical results of phase-1 cases, and a good agreement between them is achieved for all Mach number cases considered. As for the phase-3 shock, surprisingly, ε remains nearly a constant independent of the shock Mach number. It indicates that for the rippled shocks at phase 3, the instability growth contributed by the impulsive perturbation is a certain percentage of the total perturbation growth regardless of the shock strength. We stress that the present findings are applicable only for weak rippled shock cases ($M_S < 1.8$).

To quantify the difference between the present nonstandard RM instability and the standard counterpart, the amplitude growth rate obtained in this work is compared with the impulsive model of Richtmyer [1]:

$$\left(\frac{da_1}{dt}\right)_{\text{Richtmyer}} = ka^* u_1 A^*, \quad (9)$$

where A^* denotes the postshock Atwood number, and a^* is the postshock interfacial perturbation amplitude. Here the initial amplitude of the rippled shock is adopted as the interfacial

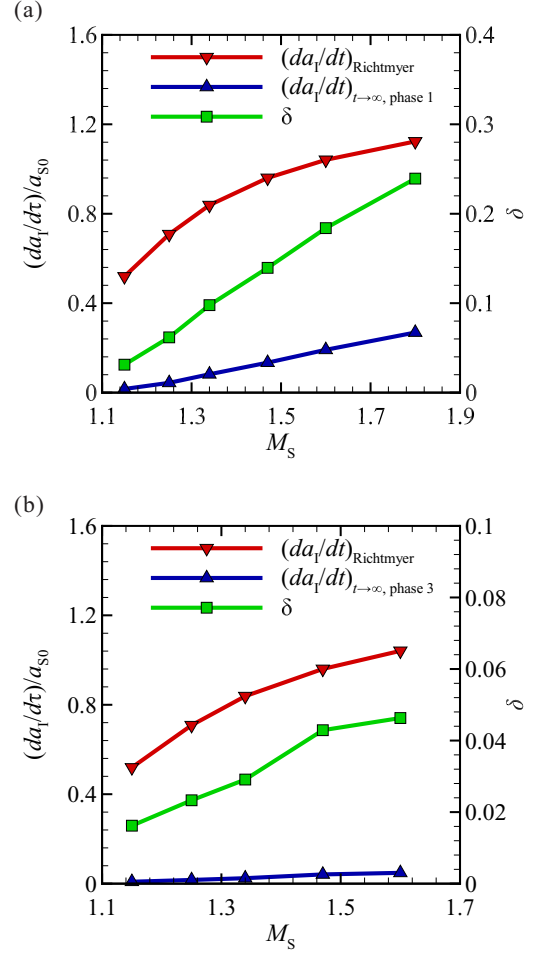


FIG. 11. Comparison of the asymptotic growth rate between the present numerical results and the impulsive model prediction for the phase-1 (a) and phase-3 (b) cases. The delta denotes the asymptotic growth rate obtained in Figs. 6 and 9. The gradient stands for the theoretical results calculated based on the impulsive model, and the square for the ratio of the above two growth rates $\delta = [(da_1/dt)_{t \rightarrow \infty}] / [(da_1/dt)_{\text{Richtmyer}}]$.

amplitude required in Eq. (9). As can be seen in Fig. 11, both $(da_1/dt)_{t \rightarrow \infty}$ and $(da_1/dt)_{\text{Richtmyer}}$ rise as the shock intensity is increased. For each case, the latter is much greater than the former, and $\delta = [(da_1/dt)_{t \rightarrow \infty}] / [(da_1/dt)_{\text{Richtmyer}}]$ increases continually with the Mach number. It indicates that the Mach number effect on the present nonstandard instability is more significant than the standard counterpart.

IV. CONCLUSION

In this work, the development of a planar N_2 - SF_6 interface subjected to a sinusoidal rippled shock has been studied through the high-resolution numerical simulation in the single-mode framework. The sinusoidal shock is generated by a planar incident shock penetrating through a sinusoidal He- N_2 interface. The characteristic of the rippled shock is carefully examined and found to agree well with the Bates' prediction, which demonstrates a good reliability of the present rippled shock generation method. Special attention is

paid to the development of the uniform interface subjected to a rippled shock at four different phases. It is found that the rippled shocks at phases 1 and 3 with a flat front cause a considerable instability growth, whereas no evident perturbation development can be observed for the phases-2 and -4 shocks with a distorted front. These phenomena are different from the standard RM instability. The high sensitivity of the instability growth to the incident shock phase can be reasonably explained by the physical mechanisms including the impulsive nonuniform and continuous pressure perturbations.

Various rippled shocks with different Mach numbers ranging from 1.15 to 1.80 are also considered to carefully study the shock strength influence on the instability growth. It is found that the influence of the shock strength on the instability growth behaves differently for rippled shocks at different phases. Specifically, for the phase-1 cases, as the rippled shock strength increases, the impulsive perturbation plays a more and more important role in the instability growth. Nevertheless, for the phase-3 cases, the instability growth

contributed by the impulsive perturbation is a certain percentage of the total growth regardless of the shock strength. The role of the impulsive perturbation in the total perturbation growth can be well predicted by an empirical formula combined with the model of Ishizaki *et al.* [17]. Comparison of the numerical growth rate with the impulsive model prediction suggests that the nonstandard instability considered here is more sensitive to the incident shock strength than the standard counterpart. The present findings are useful for better understanding complicated RM instabilities where both the shock and interface possess an initial perturbation.

ACKNOWLEDGMENTS

This work was supported by the Science Challenge Project (Grants No. TZ2016001) and the National Natural Science Foundation of China (Grants No. 11472253, No. 11602247 and NSAF U1530103). The authors are grateful to Dr. Zhigang Zhai for helpful discussions.

-
- [1] R. D. Richtmyer, *Commun. Pure Appl. Math.* **13**, 297 (1960).
 - [2] E. E. Meshkov, *Fluid Dyn.* **4**, 101 (1969).
 - [3] M. Brouillette, *Annu. Rev. Fluid Mech.* **34**, 445 (2002).
 - [4] D. Ranjan, J. Oakley, and R. Bonazza, *Annu. Rev. Fluid Mech.* **43**, 117 (2011).
 - [5] M. Vandenboomgaerde, P. Rouzier, D. Souffland, L. Biamino, G. Jourdan, L. Houas, and C. Mariani, *Phys. Rev. Fluids* **3**, 014001 (2018).
 - [6] Z. Zhai, L. Zou, Q. Wu, and X. Luo, *Proc. IMechE Part C: J. Mech. Eng. Sci.* **232**, 2830 (2018).
 - [7] J. H. J. Niederhaus, J. A. Greenough, J. G. Oakley, D. Ranjan, M. H. Andeson, and R. Bonazza, *J. Fluid Mech.* **594**, 85 (2008).
 - [8] J. A. McFarland, D. Reilly, W. Black, J. A. Greenough, and D. Ranjan, *Phys. Rev. E* **92**, 013023 (2015).
 - [9] T. Oggian, D. Drikakis, D. L. Youngs, and R. J. Williams, *J. Fluid Mech.* **779**, 411 (2015).
 - [10] Q. Zhang and W. Guo, *J. Fluid Mech.* **786**, 47 (2016).
 - [11] K. O. Mikaelian, *Phys. Rev. Fluids* **1**, 033601 (2016).
 - [12] D. Bond, V. Wheatley, R. Samtaney, and D. I. Pullin, *J. Fluid Mech.* **833**, 332 (2017).
 - [13] P. Dimotakis, *Annu. Rev. Fluid Mech.* **37**, 329 (2005).
 - [14] J. D. Lindl, O. Landen, J. Edwards, E. Moses, and N. Team, *Phys. Plasmas* **21**, 020501 (2014).
 - [15] Y. Zhou, *Phys. Rep.* **720–722**, 1 (2017).
 - [16] Y. Zhou, *Phys. Rep.* **723–725**, 1 (2017).
 - [17] R. Ishizaki, K. Nishihara, H. Sakagami, and Y. Ueshima, *Phys. Rev. E* **53**, R5592 (1996).
 - [18] C. C. Joggerst, A. Almgren, and S. E. Woosley, *Astrophys. J.* **723**, 353 (2010).
 - [19] J. O. Kane, H. F. Robey, B. A. Remington, R. P. Drake, J. Knauer, D. D. Ryutov, H. Louis, R. Teyssier, O. Hurricane, D. Arnett, R. Rosner, and A. Calder, *Phys. Rev. E* **63**, 055401(R) (2001).
 - [20] L. Zou, J. Liu, S. Liao, X. Zheng, Z. Zhai, and X. Luo, *Phys. Rev. E* **95**, 013107 (2017).
 - [21] Y. Liang, J. Ding, Z. Zhai, T. Si, and X. Luo, *Phys. Fluids* **29**, 086101 (2017).
 - [22] Z. Zhai, Y. Liang, L. Liu, J. Ding, X. Luo, and L. Zou, *Phys. Fluids* **30**, 046104 (2018).
 - [23] R. Abgrall, *J. Comput. Phys.* **125**, 150 (1996).
 - [24] E. Johnsen and T. Colonius, *J. Comput. Phys.* **219**, 715 (2006).
 - [25] V. Coralic and T. Colonius, *J. Comput. Phys.* **274**, 95 (2014).
 - [26] E. Johnsen and T. Colonius, *J. Fluid Mech.* **629**, 231 (2009).
 - [27] G. Xiang and B. Wang, *J. Fluid Mech.* **825**, 825 (2017).
 - [28] J. Meng and T. Colonius, *J. Fluid Mech.* **835**, 1108 (2018).
 - [29] W. Zhang, L. Zou, X. Zheng, and B. Wang, *Shock Waves* (2018), doi: 10.1007/s00193-018-0828-y.
 - [30] J. W. Bates, *Phys. Rev. E* **69**, 056313 (2004).